

## Circuits for light in holographically defined photonic-band-gap materials

Timothy Y. M. Chan and Sajeev John

*Department of Physics, University of Toronto, 60 St. George Street, Toronto, Ontario, M5S 1A7, Canada*

(Received 14 April 2008; published 9 September 2008)

We present a theoretical roadmap for three-dimensional optical waveguide networks in holographically defined, diamondlike photonic band gap (PBG) materials. A fully 3D waveguide network is demonstrated through broadband (100–200 nm), single-mode waveguiding in air, coupled with sharp bends in three dimensions with minimal backscattering. Optimal waveguides in the in-plane  $x$  and  $y$  directions are shown to exhibit nearly 250 nm of single-mode bandwidth for light of wavelengths near  $1.5 \mu\text{m}$ . Vertical waveguide channels are formed by introducing air defects in a zigzag pattern. Realization of these circuit designs may be achieved through the combination of direct laser writing of defects within the holographically defined photoresist and the subsequent replication of the microchip template with a high refractive index semiconductor such as silicon.

DOI: [10.1103/PhysRevA.78.033812](https://doi.org/10.1103/PhysRevA.78.033812)

PACS number(s): 42.70.Qs, 42.82.Et

### I. INTRODUCTION

Photonic band gap (PBG) materials are periodically ordered, artificial, dielectric microstructures that facilitate the localization of light with wavelengths comparable to the lattice periodicity of the structure [1,2]. When the interference effects from the periodic lattice and the microcavity scattering resonances from the individual dielectric “atoms” in a single unit cell are tuned appropriately, electromagnetic waves of a certain spectral region are forbidden from propagating in any direction [2,3]. This enables light confinement in carefully engineered defects in the photonic crystal (PC). From a practical point of view, one of the most exciting potential applications of photonic crystals is in the area of information processing. Traditionally, electron transport mechanisms in semiconductors have been used to perform the computing, storage, and transfer tasks required in this technology. However, these electronic mechanisms suffer from high heat generation and significant cross-talk between channels due to the interactions between electrons, shortcomings that become increasingly important as the size of information processing components decreases. On the other hand, photons do not in general interact with one another, except in nonlinear processes significant only under specific conditions. In addition to limiting cross-talk, this allows for increased bandwidth in multiwavelength photonic channels. The amount of heat generated in a photonic crystal-based optical device is also low, due to low absorption of light in the material. The unique characteristics of PBG materials make them an attractive and robust platform for integrating active and passive devices in an all-optical microchip.

A fundamental requirement for an all-optical microchip is the existence of waveguides to transport light throughout various points in the chip. Conventional dielectric guides based on total internal reflection are restricted by radiation loss as light is guided around sharp bends with radii of curvature on the order of the wavelength of the guided light. On the other hand, waveguides based on light localization stemming from the existence of a complete PBG can have sharp, low-loss bends [4–7]. This is achieved by introducing defects into the periodic structure of the photonic crystal, al-

lowing for localized modes with frequencies inside the PBG. When a waveguide is formed by the removal of dielectric material from the photonic crystal, the majority of the electromagnetic field in the localized mode is concentrated in air [8]. As a result, the loss from absorption is low, and therefore the main source of loss can be only from reflection at the end of the waveguide. Extending the waveguide network to all three spatial dimensions provides a paradigm for ultradense optical integrated circuits [9,10].

Recently, holographic lithography has been suggested as an approach to large scale synthesis of 3D photonic crystals by the exposure of a photoresist by a 3D optical interference pattern [11–13]. A diamondlike 3D PC lattice can be imprinted in the photoresist using a single exposure from multiple laser beams [14–18], or from a single beam diffracting through an optical phase mask [19]. An important question is whether the PBG architecture, defined by holographic lithography, can serve as a backbone for high-bandwidth, single-mode, optical waveguides and ultradense optical integrated circuitry. In this paper, we introduce design rules for creating 3D waveguide circuits with sharp, low-loss bends in this photonic crystal.

Early studies of waveguide networks based on light localization by a PBG focused on two-dimensional (2D) structures [4,20,21] that are easy to fabricate in the optical and infrared regimes. These 2D networks, however, only confine light in a plane. Confinement in the third dimension can be achieved by using finite thickness 2D slabs and limiting the waveguide modes to those “nonleaky” modes that can be confined by total internal reflection [22,23]. However, waveguide networks based on 2D PC slabs are susceptible to disorder and unintentional defects in the structure, leading to light leakage out of the plane. In contrast, waveguide networks in 3D photonic crystals offer robust PBG-based light confinement in all spatial dimensions. Designs of single-mode, air waveguide networks have been proposed for the woodpile structure [6,7,24]. Here, the layer-by-layer architecture allows for the natural inclusion of defects during the fabrication process [25]. A photonic band gap heterostructure, consisting of parallel 2D PC microchip layers separated by 3D PBG cladding layers [26,27] enables the incorporation of parallel 2D waveguide networks linked by vertical

waveguides in the cladding layers [9,10]. Templates for these heterostructures have been fabricated using direct laser writing (DLW). In DLW two-photon absorption causes exposure of a photoresist [28]. The DLW process, in which discrete volume elements of the photoresist are exposed sequentially, is amenable to the inclusion of defects in the otherwise periodic structure. However, sequential fabrication inherent to DLW is inefficient in the construction of the background PBG material. On the other hand, holographic lithography techniques offer the ability to create large 3D PBG materials with long range order, efficiently and at low cost, but do not provide an obvious route to the inclusion of predetermined defects in the periodic lattice. The 3D optical interference pattern used to create a diamondlike structure consists of only four sinusoidal terms comprising the intensity pattern. In contrast, a well defined, localized defect in the periodic lattice requires a large number of Fourier terms. This would require a correspondingly large number of beams to create the desired interference pattern. Instead, it has been suggested that an undeveloped photoresist, already patterned with holographic lithography, could subsequently be exposed using DLW to create defects [29].

In this paper, we present designs for single mode, air waveguide channels in the diamondlike structure, that can be achieved by suitable alignment of the (parallel) holographic and (serial) direct laser writing methods. We also establish design rules for sharp waveguide bends, enabling the creation of a full 3D waveguide network, exhibiting greater than 98% transmission over a 90 nm bandwidth for in-plane bends, and a 75 nm bandwidth for bends into the vertical dimension. In Sec. II, we briefly review the periodic backbone structure and describe the computational techniques and parameters used. In Sec. III we consider the design of waveguides in the diamond background structure in various crystallographic directions. In Sec. IV, we develop design rules for nearly lossless waveguide bends obtained by forming junctions between waveguides in different directions.

## II. DESIGN PARAMETERS

We consider the diamondlike optical intensity pattern described in Refs. [14–19], defined by

$$I(\vec{r}) = I_0 + C\Delta I(\vec{r}), \quad (1)$$

where  $I_0$  and  $C$  are constants depending on the particular phase mask or multibeam configuration used, and

$$\begin{aligned} \Delta I(\vec{r}) = & \cos\left[\frac{2\pi}{a}(x+z/\sqrt{2})\right] + \cos\left[\frac{2\pi}{a}(x-z/\sqrt{2})\right] \\ & + \cos\left[\frac{2\pi}{a}(y+z/\sqrt{2})\right] - \cos\left[\frac{2\pi}{a}(y-z/\sqrt{2})\right]. \quad (2) \end{aligned}$$

This intensity pattern has tetragonal Bravais lattice symmetry with aspect ratio  $c/a = \sqrt{2}$ , where  $c$  is the lattice constant in the vertical direction. We focus on the varying part of the intensity pattern, Eq. (2). After replication of the developed photoresist with a high index material, the resulting photonic crystal consists of solid material in the regions where  $\Delta I(\vec{r})$  either exceeds or falls below some threshold  $I_{\text{thr}}$ . For con-

creteness, we consider the latter scenario, corresponding to the situation where the regions exposed by DLW become air defects in the final silicon photonic crystal.

Air regions can be achieved where DLW exposure is focused by a modification of the recently established double inversion technique for SU-8 photoresist templates. In the original fabrication protocol [30], the SU-8 template is fully infiltrated by room temperature chemical vapor deposition (CVD) of  $\text{SiO}_2$  and the SU-8 removed by plasma etching or calcination in air. The inverted  $\text{SiO}_2$  template is then infiltrated by Si CVD and the  $\text{SiO}_2$  removed by chemical etching, producing a silicon replica of the over-exposed regions of the photoresist. A modified fabrication protocol can be employed to produce a silicon replica of the underexposed regions. In this new protocol [31], the first infiltration step is modified to produce only a thin shell of  $\text{SiO}_2$  surrounding the SU-8 template. Subsequent Si infiltration then creates an inverse of the original polymer template.

We choose  $I_{\text{thr}} = -1.4$  so that the solid regions of the final PBG material are characterized by  $\Delta I(\vec{r}) < -1.4$  and the air regions by  $\Delta I(\vec{r}) > -1.4$ . The equivalent but inverted structure (air and solid regions interchanged) can be obtained by setting  $I_{\text{thr}} = +1.4$  and translating the origin by  $(a/2, a/2, 0)$ . This structure has a solid volume fraction of approximately 21% and exhibits a 25% 3D PBG (relative to the center frequency of the PBG) when the solid regions consist of silicon, with dielectric constant 11.9.

*Computational methods.* Photonic band structures in this paper are calculated using the plane wave expansion method (PWEM) [32]. For the bulk PC with no defects, over 2600 plane waves are used, and Fourier coefficients are obtained using a discrete Fourier transform with 512 points per direction. The band frequencies obtained differ by less than 0.3% from those obtained using over 4300 plane waves. Waveguide modes are calculated using a supercell technique, with 1 unit cell in the waveguide direction and 6 unit cells in the other two directions, using 9000 plane waves in the PWEM. This creates, in effect, a periodic structure with parallel waveguide channels repeating in intervals of 6 unit cells. Convergence is realized when the waveguide dispersion relations become independent of the size of the supercell. Fourier coefficients are obtained using 128 points per unit cell

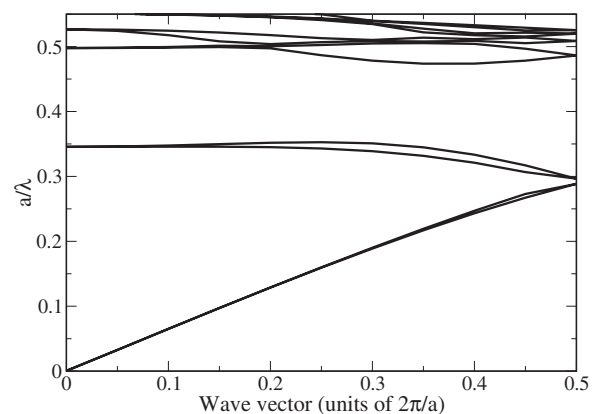


FIG. 1. Photonic band structure for the diamondlike PC, for Bloch vectors along the  $x$  and  $y$  directions.

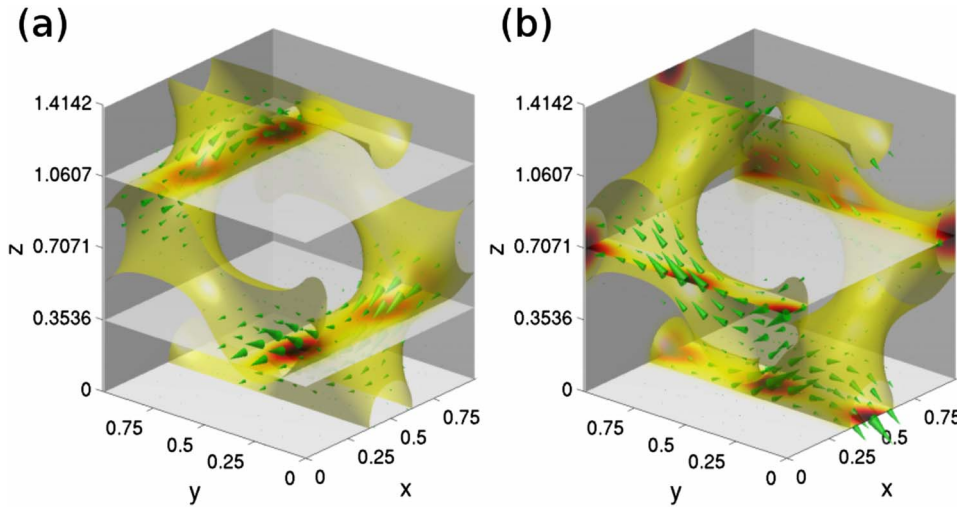


FIG. 2. (Color online) Electric displacement field for the diamondlike PC, for Bloch vectors along the  $x$  and  $y$  directions with length  $0.25[2\pi/a]$ , at an arbitrary instant in time, for the (a) third and (b) fourth bands. The field vectors are shown as arrows (green online) superimposed onto the dielectric surface of the photonic crystal in a unit cell (yellow online). High intensity regions of the field are shown in shaded dark gray (red online).

(768 points in the supercell directions). The obtained band frequencies differ by less than 1% from those obtained using over 24 000 plane waves. In addition, increasing the supercell size to 7 unit cells in the nonwaveguide directions produces less than a 0.1% change in the results, indicating the adequacy of the chosen supercell size. Light propagation through the waveguide channels is modeled using the finite-difference time-domain (FDTD) method [33] with 12 mesh points per  $a$  (unit cell in the  $x$  and  $y$  directions) and 16 mesh points per  $c$  (unit cell in the  $z$  direction). The grid spacing in the  $z$  direction is adjusted to maintain the desired aspect ratio  $c/a = \sqrt{2}$ . Transmission and reflection spectra are obtained by calculating the Poynting vector fluxes through planar surfaces perpendicular to the waveguide channels. We use planar surfaces extending over three unit cells in each direction away from the waveguide.

**III. WAVEGUIDE DESIGN**

Waveguide channels can be formed by introducing a series of defects in the photonic crystal structure. In general, the removal of material from a photonic crystal creates air modes (defined as modes in which field energy is concentrated in air) originating from the bands on the lower edge of the PBG, whereas the addition of material creates dielectric modes (defined as modes in which energy is concentrated in the solid regions of the crystal) originating from the upper band edge [8]. Following the procedure introduced in Ref. [10], we examine the electromagnetic field distributions in the originating bands of the perfect structure in order to determine the desired defect locations. Removing dielectric material in those locations where field energy is concentrated near the lower band edge mode facilitates the creation of broad bandwidth, single-mode, air waveguides. Removal of dielectric from other regions tends to produce multimode or narrow band waveguides that are much more susceptible to backscattering losses in the presence of small amounts of random disorder. A similar procedure was also used to design waveguides in a body-centered cubic holographic PC [34].

We first consider the design of air waveguides in the  $x$  and  $y$  directions. Air waveguide modes originate from those

bands of the bulk PC at the lower edge of the band gap. Figure 1 shows the photonic band structure of the bulk PC in the  $x$  and  $y$  directions, which are equivalent due to the symmetry of the structure. Figures 2(a) and 2(b) show the electric displacement field distributions for the third and fourth bands, respectively, at a Bloch vector of length  $0.25[2\pi/a]$  and some arbitrary instant in time. The shaded dark gray (red online) regions correspond to regions of high field intensity. These high intensity regions are centered at the tetrahedral “bonds” characteristic to the diamond architecture. Figure 3 shows the mode frequency of a localized state of light as a function of the sphere radius for a spherical air defect centered at  $(0, 0, 0)$ . This is equivalent to introducing an air defect centered at any of the intensity maxima in Fig. 2(a) or Fig. 2(b), due to the symmetry of the structure.

We now focus on the distribution in Fig. 2(a). The fields are clearly concentrated along lines in the  $x$  direction, with intensity maxima centered at  $(a/4, a/4, c/4)$ ,  $(3a/4, a/4, c/4)$ ,  $(a/4, 3a/4, 3c/4)$ , and  $(3a/4, 3a/4, 3c/4)$ , and field vectors pointing in the  $x$ - $z$  plane. Both our current structure and the woodpile PBG structure [35,36], as diamondlike architectures, are characterized by “nodes” of material joined by tetrahedral “bonds.” In the woodpile architecture, the dielectric nodes are centered at the meeting points between perpendicular rods. As a result, a correspon-

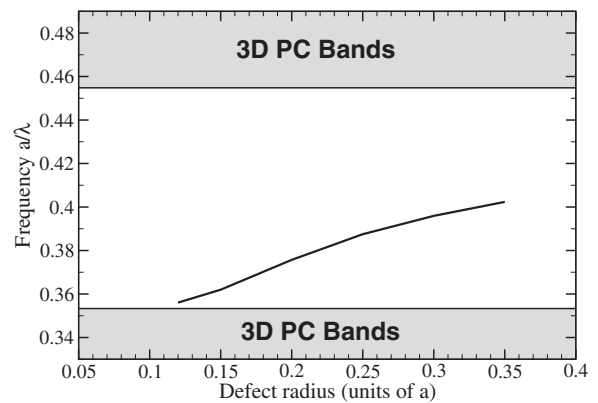


FIG. 3. Defect mode frequency for single spherical air defects as a function of the sphere radius.

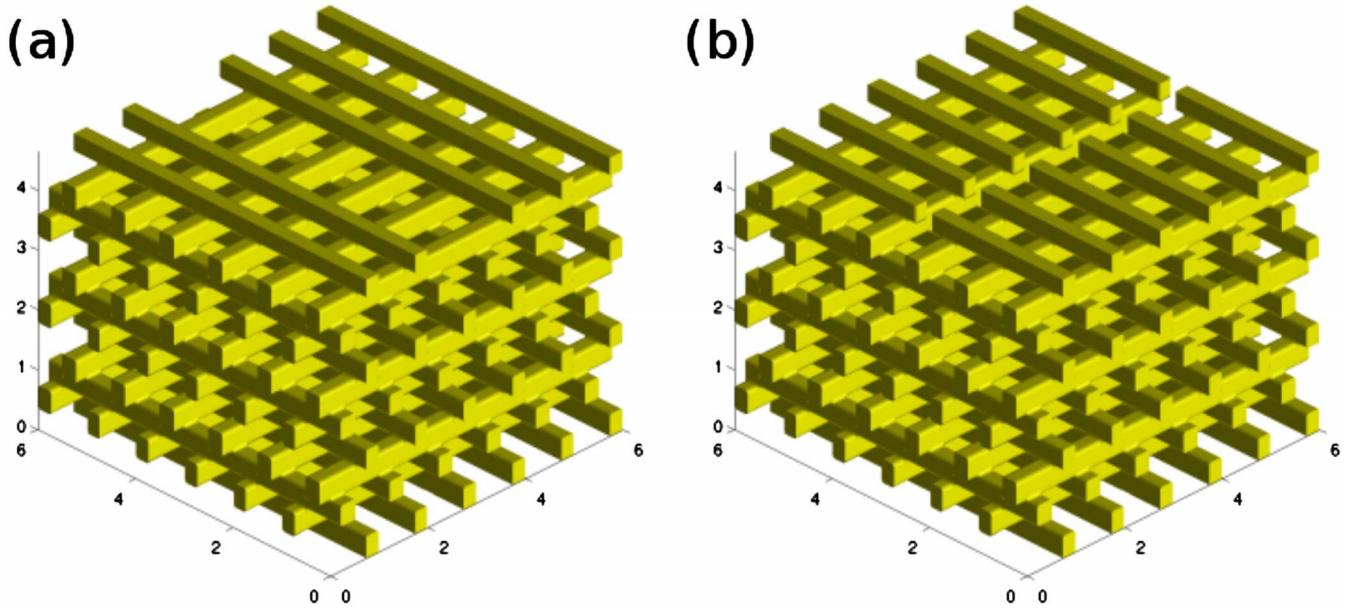


FIG. 4. (Color online) (a) Type I waveguide in the woodpile structure. The waveguide is characterized by a missing rod in the top layer shown. (b) Type II waveguide in the woodpile structure. The waveguide is characterized by a series of air defects cutting across the rods in the top layer shown.

dence can be made between the field vector lines in our holographically defined PBG material and the dielectric rods running in the  $x$  direction in the woodpile PBG structure. This suggests that waveguide channels in the  $x$  direction, with electric fields polarized in the  $x$ - $z$  plane, can be obtained by removing material around each point  $((2m+1)a/4, a/4, c/4)$  or around each point  $((2m+1)a/4, 3a/4, 3c/4)$ , where  $m$  is the sequence of integers chosen to span the desired waveguide length. We denote these waveguides as  $\mathbf{X}_{a/4c/4}^{XZ}$  and  $\mathbf{X}_{3a/43c/4}^{XZ}$ , respectively, where the superscript indicates the plane of polarization and the subscript indicates the  $y$  and  $z$  coordinates of the defect centers. These waveguides correspond to removing a single rod to create a waveguide channel in the woodpile structure. We refer to these waveguides that follow the field vector lines as type-I waveguides. Figure 4(a) shows a type-I waveguide in the woodpile PBG material. Similarly, the field patterns in Fig. 2(b) suggest that waveguides in the  $y$  direction, with field vectors in the  $y$ - $z$  plane, can be obtained by removing material around  $(a/2, ma/2, 0)$  or  $(0, ma/2, c/2)$ . In our naming scheme, these waveguides are denoted as  $\mathbf{Y}_{a/20}^{YZ}$  and  $\mathbf{Y}_{0c/2}^{YZ}$ , respectively.

As a detailed illustration of a type-I waveguide, we investigate the case where material is removed around the points  $((2m+1)a/4, a/4, c/4)$ , creating a waveguide in the  $x$  direction  $\mathbf{X}_{a/4c/4}^{XZ}$ . The other cases, for both the  $x$  and  $y$  directions, are analogous due to the symmetry of the structure. For simplicity, we assume that material is removed from spheres centered at the intensity maxima. Further optimization of the waveguide single-mode bandwidth may be possible using defects better tailored to the ellipsoidal shape of the high intensity regions. Figure 5(a) shows the waveguide with removed regions of the periodic backbone indicated by dark gray (red online). The radius of the air spheres is  $0.25a$ . We find that this choice of radius maximizes the bandwidth of

the waveguide mode without introducing undesired modes. Due to the linear nature of the waveguide, these spherical defects could be replaced by a cylindrical air hole with matching radius, passing through the centers of the spheres. The additional material removed would not disturb any additional high field intensity regions in Fig. 2, so the waveguide mode would not be altered significantly. The corresponding waveguide band structure is shown in Fig. 5(b).

The removal of material from the periodic structure creates air modes originating from the lower edge of the PBG. In this case, the waveguide mode is created by disturbing two high field intensity regions per unit cell in the waveguide direction. As a result, the waveguide mode consists of two bands, originating from the first and third bands in the periodic structure. These are the bands in the periodic structure whose electromagnetic mode field patterns are polarized in the  $x$ - $z$  plane, as is the waveguide mode. The single-mode region of the waveguide mode spans the normalized frequency range  $a/\lambda \sim 0.354-0.401$ , corresponding to a bandwidth of 199 nm if the waveguide mode is centered at  $1.5 \mu\text{m}$  ( $a \sim 600 \text{ nm}$ ). The group velocity of light in the waveguide with Bloch vector near  $0.4[2\pi/a]$  reaches approximately 0.15 times the speed of light in vacuum. This group velocity is somewhat lower than the group velocity attained in the corresponding waveguide of a 2D-3D PBG heterostructure [26].

In addition to waveguide channels that follow the lines of concentrated field intensity, it is also possible to create waveguides that cut across these lines. We refer to these channels as type-II waveguides. This involves the creation of one defect per unit cell along the direction orthogonal to the field vector lines. For a type-II waveguide in the  $y$  direction, the defect can be centered at any of the high field intensity regions in Fig. 2(a), provided the defect is repeated along the  $y$  direction. Creating air defects at any of the high intensity

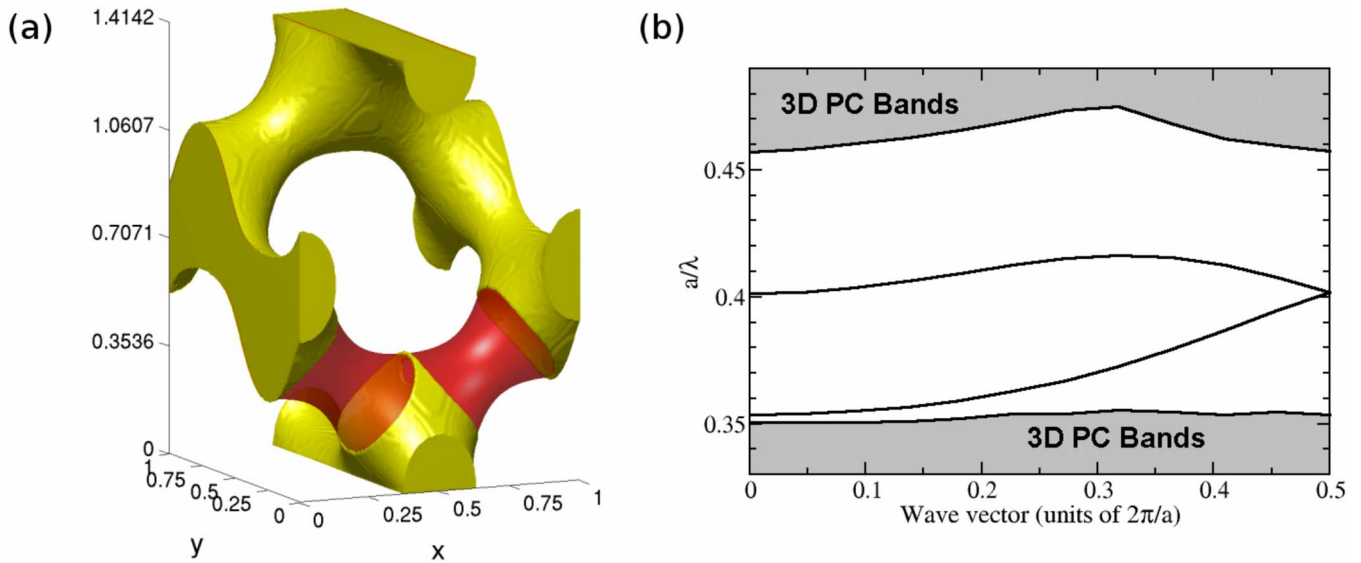


FIG. 5. (Color online) (a) Waveguide in the  $x$  direction  $\mathbf{X}_{a/4c/4}^{XZ}$ , with material removed at spheres of radius  $0.25a$  centered at  $((2m+1)a/4, a/4, c/4)$ . The removed regions are indicated by dark gray (red online). (b) Corresponding dispersion relation. The single-mode region of the waveguide mode (frequency range over which there is only one mode) spans the normalized frequency range  $a/\lambda \sim 0.354 - 0.401$ .

regions in Fig. 2(b), with the appropriate periodicity, leads to a waveguide in the  $x$  direction. Figure 6(a) shows a two unit cells of a waveguide channel in the  $y$  direction created by spherical defects of radius  $0.30a$  centered at  $(a/4, (4m+1)a/4, c/4)$ , with the removed regions of the periodic structure in dark gray (red online). In our classification scheme, this waveguide is denoted  $\mathbf{Y}_{a/4c/4}^{XZ}$ , as the electric fields for this waveguide mode are polarized in the  $x-z$  plane. Figure 6(b) shows the corresponding waveguide band structure, consisting of a single, monotonic band spanning the normalized frequency range  $a/\lambda \sim 0.370 - 0.436$ . If the cen-

ter wavelength is  $\lambda = 1.5 \mu\text{m}$ , this corresponds to a bandwidth of 245 nm. This waveguide is analogous to the “type-II  $Y$ ” waveguide in woodpile photonic crystals studied by Li and Ho [24], except that the bandwidth in our case is wider due to the larger PBG of the holographic diamond structure [39]. Figure 4(b) shows a type-II waveguide in the woodpile PBG material. The group velocity of light in the waveguide with Bloch vector near  $0.3 [2\pi/a]$  reaches approximately 0.22 times the speed of light in vacuum. This is nearly the group velocity attained in the in-plane waveguides of 2D-3D PBG heterostructures [26].

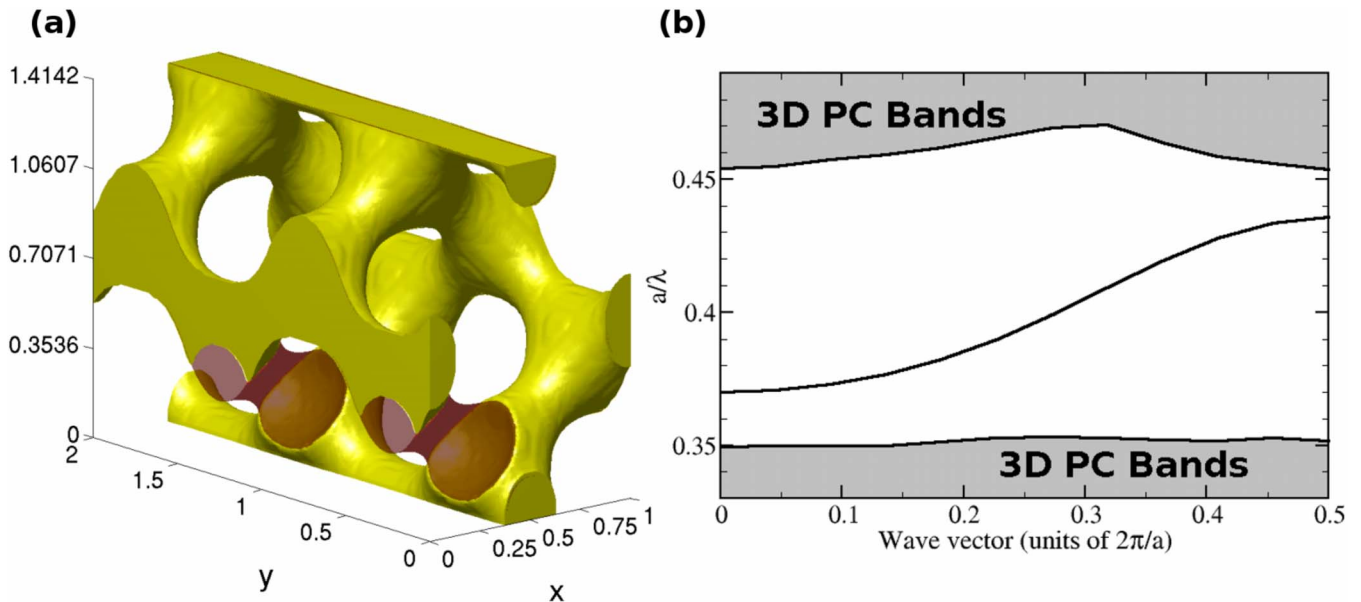


FIG. 6. (Color online) (a) Alternative waveguide in the  $y$  direction  $\mathbf{Y}_{a/4c/4}^{XZ}$ , with material removed at spheres of radius  $0.30a$  centered at  $(a/4, (4m+1)a/4, c/4)$ . The removed regions are indicated by dark gray (red online). (b) Corresponding dispersion relation. The waveguide mode spans the normalized frequency range  $a/\lambda \sim 0.370 - 0.436$ , corresponding to 245 nm when the central wavelength is  $1.5 \mu\text{m}$ .

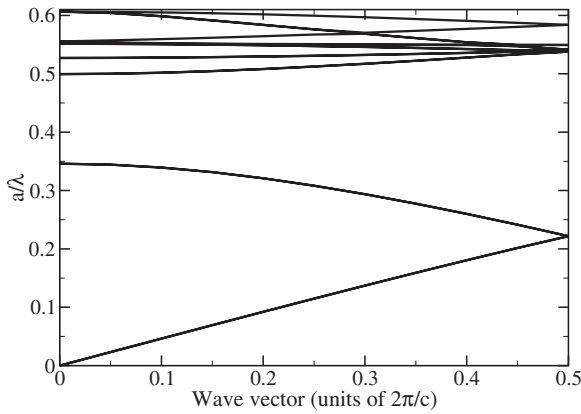


FIG. 7. Photonic band structure for the diamondlike PC for Bloch vectors in the  $z$  direction.

Waveguides in the vertical ( $z$ ) direction can also be designed by examining the band structure and field distributions for waves propagating in the  $z$  direction near the lower edge of the complete PBG. Figure 7 shows the band structure

for the unaltered PC along the  $z$  direction. There are two doubly degenerate pairs of bands below the PBG. The field intensity distributions closely resemble the distributions for Bloch vectors in the  $x$  and  $y$  directions, with intensity maxima occurring at the same locations as in the previous case. However, there is no high-bandwidth waveguide obtained by removing material in a straight line in the vertical direction. In analogy with 2D-3D heterostructures [9,10], a zigzag pattern of dielectric removal must be used. For concreteness, we consider removing material at the intensity maxima shown in Fig. 2(a). In this case, the intensity maxima are found at  $(a/4, a/4, c/4)$ ,  $(3a/4, a/4, c/4)$ ,  $(a/4, 3a/4, 3c/4)$ , and  $(3a/4, 3a/4, 3c/4)$ . A vertical waveguide can be formed by (1) removing regions centered at a constant  $x$  coordinate, such as at  $(a/4, a/4, c/4)$ ,  $(a/4, 3a/4, 3c/4)$ , and so on [shown in Fig. 8(a)], (2) removing regions centered at a constant  $y$  coordinate, such as at  $(a/4, a/4, c/4)$ ,  $(a/4, a/4, 5c/4)$ , and so on [Fig. 8(b)], or (3) removing regions without keeping  $x$  or  $y$  constant, such as at  $(a/4, a/4, c/4)$ ,  $(3a/4, 3a/4, 3c/4)$ , and so on [Fig. 8(c)].

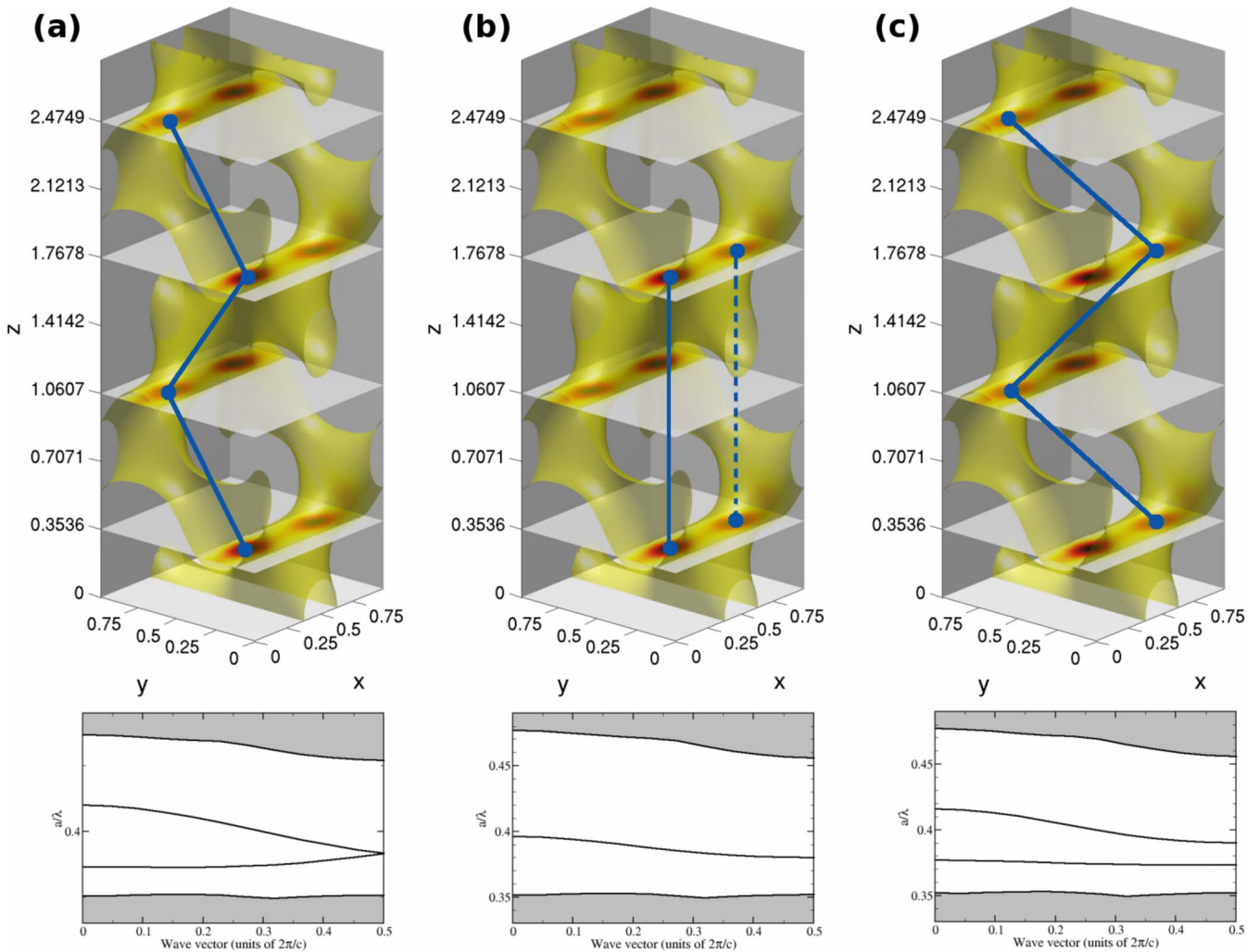


FIG. 8. (Color online) Possible schemes for creating vertical waveguides with electric fields polarized in the  $x$ - $z$  plane, with corresponding band structures shown below: (a) Removing regions centered at a constant  $x$  coordinate, (b) removing regions centered at a constant  $y$  coordinate, and (c) removing regions without keeping  $x$  or  $y$  constant.

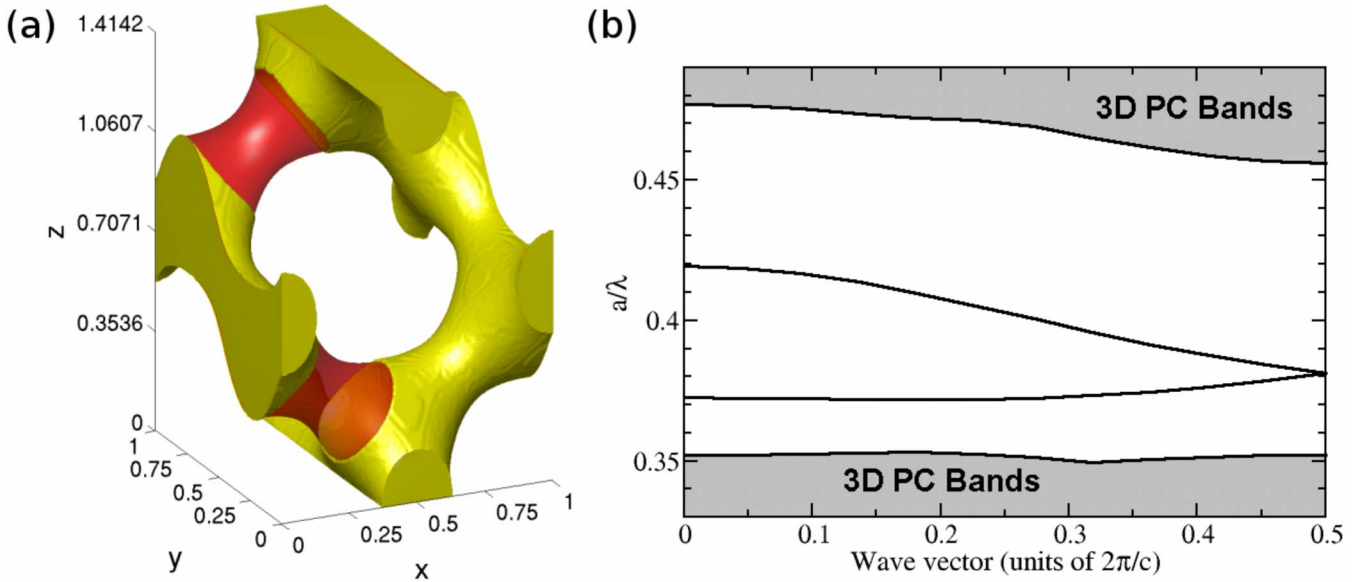


FIG. 9. (Color online) (a) Waveguide in the  $z$  direction  $\mathbf{Z}_{x=a/4}^{XZ}$  with material removed at spheres of radius  $0.25a$  centered at  $(a/4, a/4, c/4)$  and  $(a/4, 3a/4, 3c/4)$  in unit cells along the  $z$  direction. The removed regions are indicated in dark gray (red online). (b) Corresponding dispersion relation. The single-mode region of the waveguide mode spans the normalized frequency range  $a/\lambda \sim 0.374 - 0.420$ .

We find that removing rods centered at constant  $x$  (case 1) maximizes the single-mode waveguiding bandwidth. For cases 2 and 3, the resulting defect modes span a narrow bandwidth. In case 2, the dispersion relation strongly resembles one obtained using a tight binding model describing the waveguide as a series of weakly coupled optical resonators with mode frequencies as shown in Fig. 3 [37]. The weak coupling is unable to produce a mode with a wide bandwidth. In order to increase the bandwidth, additional defects must be included, increasing the number of waveguide bands [34]. In cases 1 and 3, one additional defect is created per unit cell in the waveguide direction, causing the formation of a second waveguide band. In case 3, the placement of the defects creates an inversion symmetry. As a result, there is a mode gap between the two waveguide bands, which limits the bandwidth [20]. Similarly, if an additional defect is created in the locations indicated by the dotted line in Fig. 8(b), a mirror reflection plane exists at  $x=0.5a$  and a mode gap is formed between the two waveguide bands. On the other hand, the waveguide channel in case 1 lacks both inversion symmetry and a mirror reflection plane. The resultant lack of a mode gap between the two waveguide modes enables a large single-mode bandwidth.

The air waveguide for case 1 is shown in Fig. 9(a) with removed parts indicated in dark gray (red online). We denote this as the  $\mathbf{Z}_{x=a/4}^{XZ}$  waveguide in our naming scheme. An equivalent waveguide could be created by removing material at the  $x=3a/4$  regions ( $\mathbf{Z}_{x=3a/4}^{XZ}$ ). The dispersion relation for this waveguide is shown in Fig. 9(b). Again, the waveguide mode consists of two bands, the single-mode portions of which span a normalized frequency range of  $a/\lambda \sim 0.374 - 0.420$ , corresponding to a bandwidth of 175 nm if the 3D PBG is centered at  $1.5 \mu\text{m}$  ( $a \sim 600 \text{ nm}$ ). The group velocity of light in this waveguide reaches approximately 0.14 times the speed of light in vacuum. The waveguide mode created

by this defect has its electric field polarized in the  $x$ - $z$  plane. An analogous waveguide can be created by removing regions centered at a constant  $y$  coordinate from Fig. 2(b) ( $\mathbf{Z}_{y=0}^{YZ}$ ). In this case (which is the same as case 1 above rotated by  $90^\circ$  about the  $z$  axis and translated one quarter of a lattice constant in the vertical direction) the electric field is polarized in the  $y$ - $z$  plane.

#### IV. WAVEGUIDE BENDS

The existence of high-bandwidth, single-mode, linear waveguide channels in three orthogonal directions, within the holographically defined PBG backbone, offers the opportunity for circuits of light within a truly 3D optical microchip. Unlike earlier 2D-3D PBG heterostructures [26,27], which require alignment and embedding of 2D microchip layers in a 3D PBG material, the holographically defined architectures do not require an intermediate 2D photonic crystal synthesis step. However, careful alignment of the optical fields provided by the optical phase mask for creating the PBG backbone material and the optical voxels for direct laser writing of waveguides is needed. From a design point of view, it is also important to establish that sharp waveguide bends providing nearly perfect transmission of light over a large bandwidth can be engineered within the holographic diamond architecture. In this section, we establish the required design rules.

##### A. Horizontal type-I waveguide bends

We first investigate bending of light between identical waveguides in the  $x$  and  $y$  directions. We begin by studying bends between type-I waveguide channels along lines of concentrated field intensity, as shown in Fig. 5. In this case, the waveguides in the  $x$  and  $y$  directions are denoted by

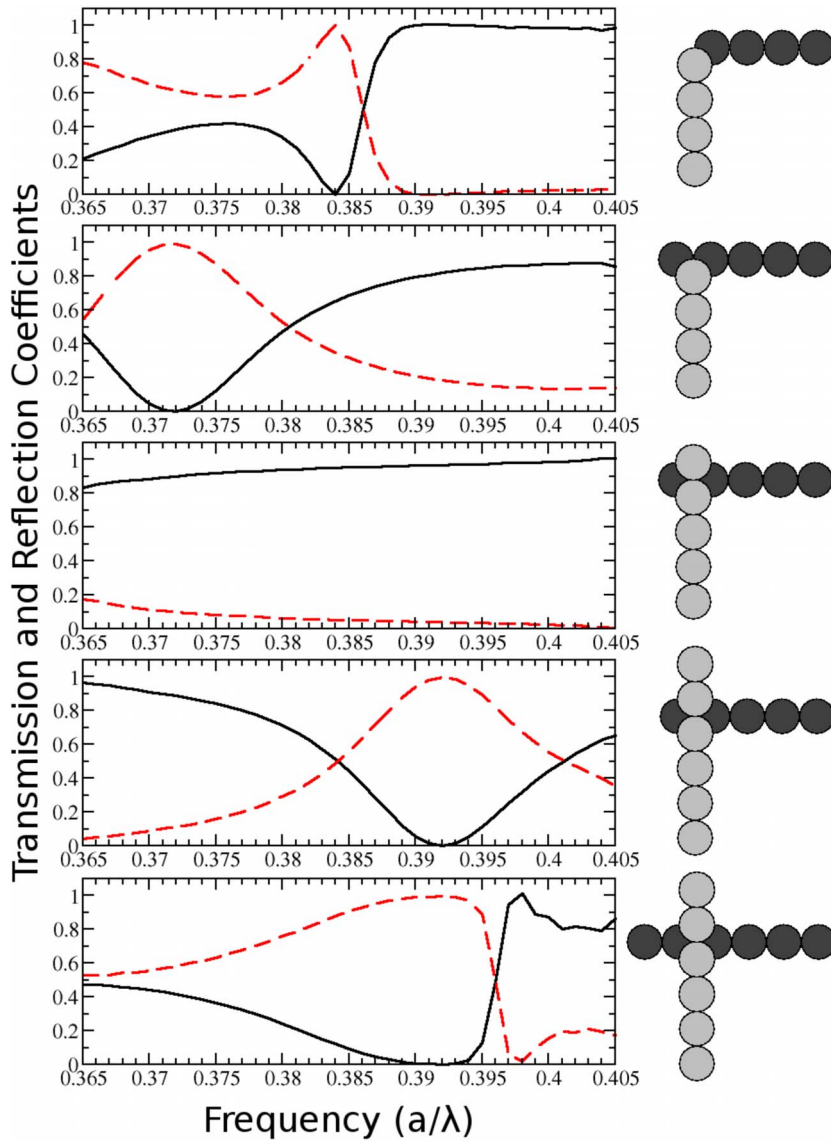


FIG. 10. (Color online) Transmission (solid, black online) and reflection (dashed, red online) spectra for bends between waveguides in the  $x$  and  $y$  directions for various bend geometries. The light gray circles in the schematic bend diagrams represent air spheres centered in the  $z=c/2$  plane, while the dark gray circles represent air spheres centered in the  $z=c/4$  plane.

$\mathbf{X}_{a/4c/4}^{XZ}$  and  $\mathbf{Y}_{0c/2}^{YZ}$ , respectively. The shape of the waveguide elbow can be modified by adjusting the termination points of each waveguide, altering the amount of overshoot between the two channels. We use a FDTD simulation to model the transmission of light through the bend using a pulse spanning the frequency range  $a/\lambda \sim 0.365-0.405$ , avoiding the flat parts of the waveguide dispersion curve (slow group velocity) and minimizing the spread of the pulse over the length of the waveguide channels. Figure 10 shows transmission and reflection spectra for various bend geometries. The configuration in which both waveguides overshoot each other by a single defect (see third panel of Fig. 10) enables over 90% transmission through the bend over the frequency range  $a/\lambda \sim 0.372-0.405$ . This corresponds to a bandwidth of about 130 nm when the PBG is centered at  $1.5 \mu\text{m}$ . Over 95% transmission is obtained throughout the frequency range  $a/\lambda \sim 0.384-0.405$  (approximately 80 nm bandwidth), and more than 98% transmission over  $a/\lambda \sim 0.398-0.405$  ( $\sim 25$  nm). In addition, the configuration with no overshoot between the two waveguides (top panel of Fig. 10) allows for over 98% transmission over the frequency range  $a/\lambda$

$\sim 0.389-0.405$  (approximately 60-nm bandwidth), at the cost of low transmission at lower frequencies.

Other bend geometries permit no transmission through the bend at certain frequencies (panels two and four in Fig. 10). Due to the bend geometries and the envelope amplitudes of the electromagnetic field at specific wave vectors, the longitudinal profiles of the waveguide mode have nodes at the position where the two channels overlap and strong reflection occurs at specific frequencies. The field in the incoming waveguide channel is unable to excite modes in the outgoing channel and light is not transmitted through the bend. The configuration in the fourth panel of Fig. 10, with a single defect overshoot in one channel, and a double defect overshoot in the second channel, can be thought of as a modification of the configuration in the third panel, with an additional side-coupled defect. Indeed, the transmission spectrum for this case corresponds closely to the transmission spectrum obtained for a straight waveguide with a single, side-coupled air cavity. By analogy, the transmission characteristics of the configuration with double defect overshoot for both waveguide channels (bottom panel of Fig. 10) are sug-

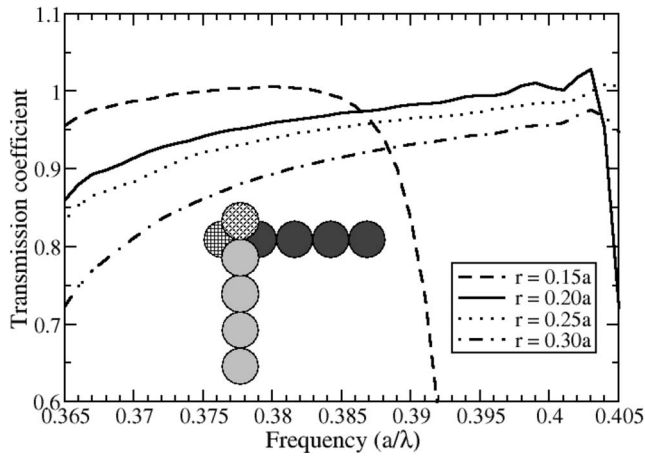


FIG. 11. Transmission spectra for bends with a single air sphere overlap between the  $x$  and  $y$  waveguide channels. The radius of the overlapping air spheres, shown with hashing in the inset, is varied. The other spheres in the body of the waveguide have radius  $0.25a$ .

gestive of a broadened reflection peak resulting from the existence of two cavities.

The transmission characteristics of the bend can be altered by further structural modification. Figure 11 shows the effect of varying the radii of the terminating air spheres (at the endpoint of each linear waveguide segment) on the transmission spectrum of the configuration with single sphere overshoot. A slight decrease of the radii of these terminating defects to  $0.20a$  from  $0.25a$  increases the transmission by  $\sim 2\%$  over a large range of frequency. Further decreasing the radius to  $0.15a$  produces over 95% transmission in the frequency

range  $a/\lambda \sim 0.365-0.387$ , at the cost of low transmission at higher frequencies. On the other hand, increasing the radii of the terminating spheres decreases the transmission over the entire spectrum.

**B. Horizontal type-II waveguide bends**

We now consider bending between type-II waveguides in the  $x$  and  $y$  directions formed by cutting across lines of concentrated field intensity, as in the waveguide channel depicted in Fig. 6. Figure 12 shows the transmission and reflection spectra for light propagating from a  $y$  waveguide channel, denoted by  $Y_{a/4c/4}^{XZ}$ , into various waveguide channels in the  $x$  direction, for a pulse spanning the frequency range  $a/\lambda \sim 0.380-0.435$ . When light from the  $Y_{a/4c/4}^{XZ}$  waveguide is coupled to a  $X_{a/2c/2}^{YZ}$  waveguide, as shown in the top panel of Fig. 12, over 90% of the light is transmitted over the frequency range  $a/\lambda \sim 0.380-0.409$ , corresponding to a bandwidth of about 110 nm for a PBG centered at  $1.5 \mu\text{m}$ . Transmission above 95% and 98% is obtained over frequency ranges  $a/\lambda \sim 0.381-0.401$  ( $\sim 80$  nm bandwidth for a PBG at 1.5-micron) and  $a/\lambda \sim 0.382-0.391$  ( $\sim 35$  nm), respectively.

If the light is instead coupled to a parallel  $x$ -waveguide channel ( $X_{ac/2}^{YZ}$ ) that is  $a/2$  farther away from the termination of the  $y$  waveguide, as shown in the middle panel of Fig. 12, the 90% transmission frequency range increases to  $a/\lambda \sim 0.386-0.435$  ( $\sim 175$  nm bandwidth). The frequency ranges for transmission above 95 and 98 % improve to  $a/\lambda \sim 0.395-0.435$  ( $\sim 140$  nm) and  $a/\lambda \sim 0.411-0.435$  ( $\sim 80$  nm), respectively.

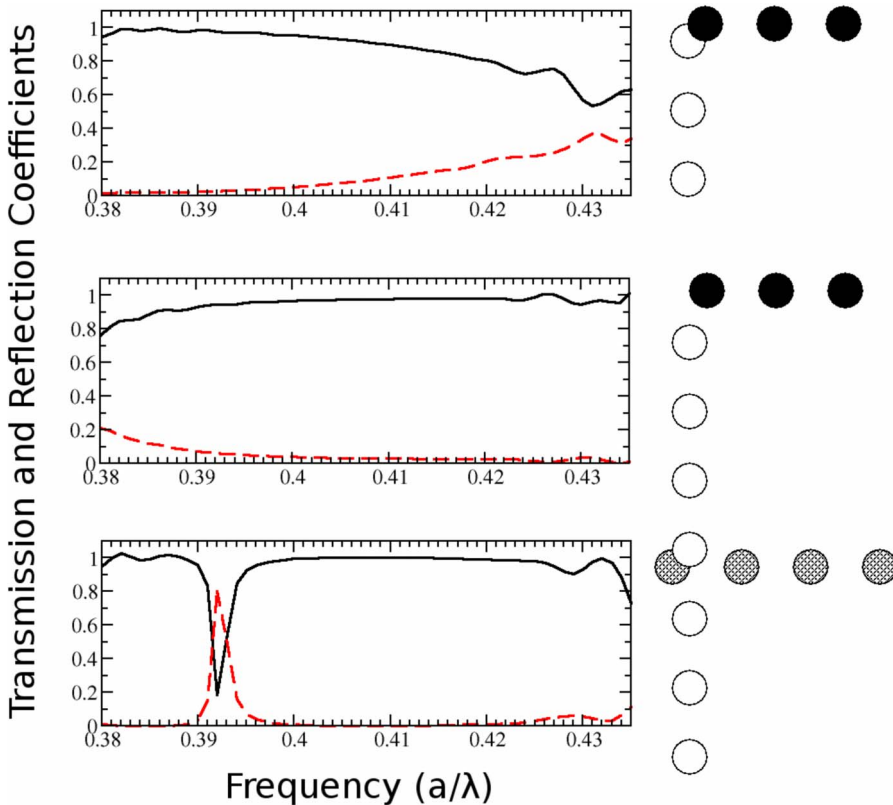


FIG. 12. (Color online) Transmission (solid, black online) and reflection (dashed, red online) spectra for bends between alternative waveguides in the  $x$  and  $y$  directions for various bend geometries. The white, black, and cross-hatched circles in the schematic bend diagrams represent air spheres centered in the  $z=c/4$ ,  $z=c/2$ , and  $z=0$  planes, respectively.

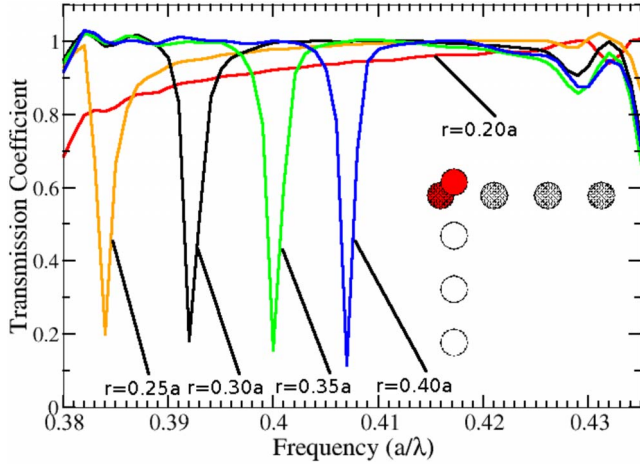


FIG. 13. (Color online) The transmission spectra for bends between  $\mathbf{Y}_{a/4c/4}^{XZ}$  and  $\mathbf{X}_{a/40}^{YZ}$  waveguides in the  $x$  and  $y$  directions, as the radii of the shaded defects (red online) are adjusted. The reflection peak is redshifted as the defect radius is decreased. The unaltered defects have radius  $0.30a$ .

The configuration shown in the bottom panel of Fig. 12, with bending between a  $\mathbf{Y}_{a/4c/4}^{XZ}$  waveguide and a  $\mathbf{X}_{a/40}^{YZ}$  waveguide, produces over 98% transmission over almost the entire frequency range studied, except around a strong reflection peak near  $a/\lambda = 0.392$ . Due to this peak, the transmission drops below 98% in the frequency range  $a/\lambda \sim 0.389 - 0.399$ . By adjusting the size of the terminating defects for each waveguide, it is possible to change the center frequency of this reflection peak, as shown in Fig. 13.

### C. Horizontal hybrid waveguide bends

Due to the existence of two types of waveguides in the  $x$  and  $y$  directions it is possible to create bends between waveguides that lie in the same  $x$ - $y$  plane. This corresponds to a link between a type-I waveguide and a type-II waveguide. Figure 14 shows the transmission and reflection spectrum for a bending configuration with no overshoot for either waveguide channel. About 90% of the light is transmitted over the frequency range  $a/\lambda \sim 0.382 - 0.405$ , representing about a 90 nm bandwidth when the 3D PBG is centered at

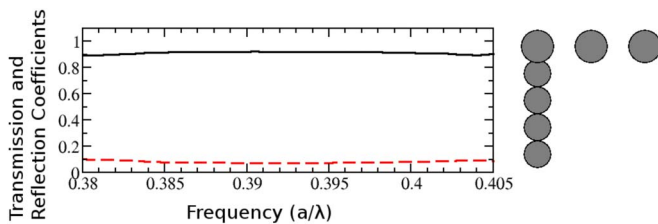


FIG. 14. (Color online) Transmission (solid, black online) and reflection (dashed, red online) spectra for a bend between coplanar waveguide channels in the  $x$  and  $y$  directions. The  $x$  waveguide channel is formed by cutting across the lines of concentrated field intensity in the periodic structure, while the  $y$  waveguide channel is formed by adding defects along these lines. The air defects in the  $x$  and  $y$  have radius  $0.30a$  and  $0.25a$ , respectively.

$1.5 \mu\text{m}$ . Other bend geometries we considered displayed inferior transmission. In addition, the bending bandwidth is inherently limited by the relatively small frequency overlap between the different waveguide modes.

### D. Vertical bends from type-I waveguides

We finally consider the bending of light from a waveguide channel in the  $x$ - $y$  plane into a waveguide channel in the vertical direction. We first investigate coupling from a type-I waveguide in the  $x$  direction comprised of defects located along the lines of concentrated field intensity of the periodic structure, as illustrated in Fig. 5. The mode associated to this waveguide channel, denoted as  $\mathbf{X}_{a/4c/4}^{XZ}$ , has its electric field polarized in the  $x$ - $z$  plane and magnetic field in the  $y$  direction. This waveguide can either be coupled to the vertical waveguide denoted by  $\mathbf{Z}_{y=0}^{YZ}$  or the one denoted by  $\mathbf{Z}_{x=a/4}^{XZ}$ . In the first case, the vertical waveguide mode has electric field polarized in the  $y$ - $z$  plane and magnetic field polarized in the  $x$  direction. When considering the field components perpendicular to the waveguide direction, neither the electric ( $\hat{z} \rightarrow \hat{y}$ ) nor magnetic field ( $\hat{y} \rightarrow \hat{x}$ ) is conserved across the bend. As a result, a bend between these waveguides results in virtually no transmission, because the field from the first waveguide is unable to excite the mode of the second waveguide [10]. The vertical waveguide denoted by  $\mathbf{Z}_{x=a/4}^{XZ}$ , on the other hand, has electric field polarized in the  $x$ - $z$  plane and magnetic field in the  $y$  direction. Here, the perpendicular components of the electric field ( $\hat{z} \rightarrow \hat{x}$ ) are still not conserved across the bend, but the magnetic field component ( $\hat{y} \rightarrow \hat{y}$ ) is conserved. Figure 15 shows the transmission and reflection spectra for various bend geometries between the  $\mathbf{X}_{a/4c/4}^{XZ}$  and  $\mathbf{Z}_{x=a/4}^{XZ}$  waveguides. As in the case of  $x$ - $y$  bends, the best case occurs when there is a single defect overshoot for both waveguide channels (see panel 2 of Fig. 15). For this geometry, we predict over 95% transmission over the frequency range  $a/\lambda \sim 0.387 - 0.405$ , corresponding to a bandwidth of approximately 70 nm when the 3D PBG is centered at  $1.5 \mu\text{m}$ . Other bend geometries either permit relatively low transmission throughout the frequency range (top panel of Fig. 15) or exhibit reflection peaks (bottom two panels of Fig. 15).

### E. Vertical bends from type-II waveguides

The bandwidth of bends between vertical waveguides and type-I waveguides shown in Fig. 5 is limited in part by the relatively small frequency overlap between the two waveguide modes. In contrast, type-II waveguides illustrated in Fig. 6 are better matched in frequency with the vertical waveguides we have defined. We consider bends into the vertical direction from a type-II waveguide in the  $x$  direction denoted by  $\mathbf{X}_{a/2c/2}^{YZ}$ . The electric field of this waveguide mode is polarized roughly along a diagonal in the  $y$ - $z$  plane. The magnetic field likewise has nonzero components in both the  $y$  and  $z$  directions. As a result, it is possible to couple between this waveguide and either orientation of the zigzag vertical waveguide. Figure 16 shows the transmission and reflection spectra for bends into vertical waveguides where the zigzag pattern is formed at a constant  $x$  coordinate. In this case, the vertical waveguide mode has its electric field

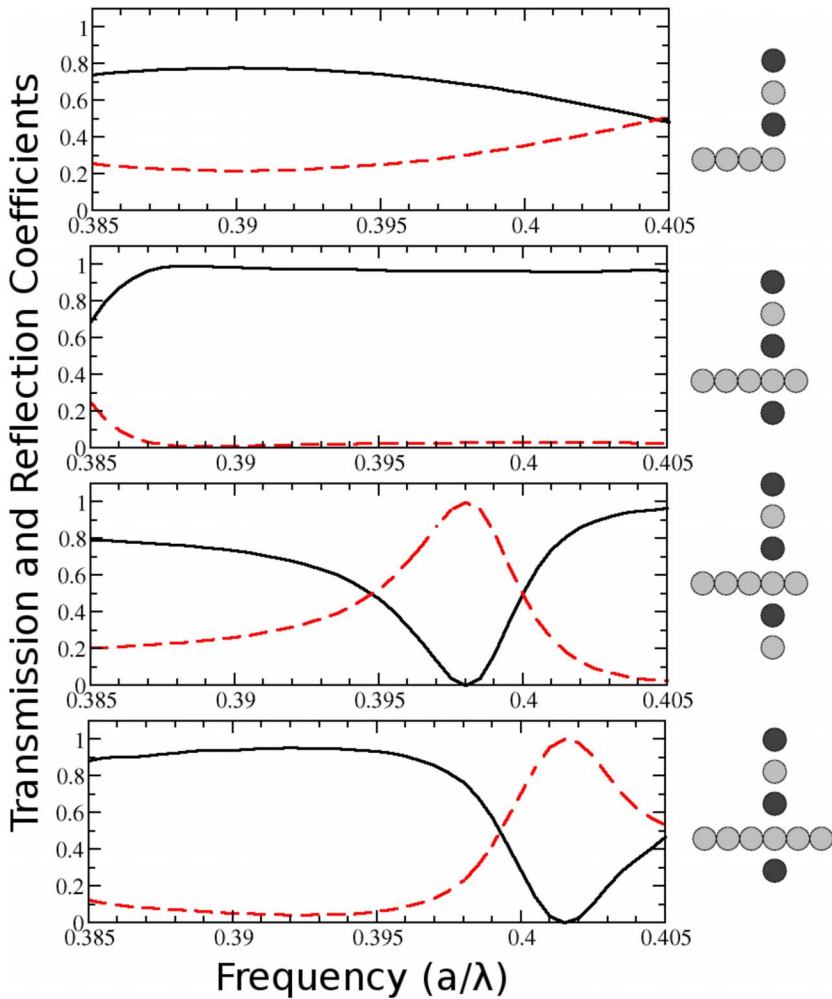


FIG. 15. (Color online) Transmission (solid, black online) and reflection (dashed, red online) spectra for bends between waveguides in the  $x$  (horizontal) and  $z$  (vertical) directions for various bend geometries. The light gray circles in the schematic bend diagrams represent air spheres centered in the  $y=a/4$  plane, while the dark gray circles represent air spheres centered in the  $y=3a/4$  plane.

polarized in the  $x$ - $z$  plane. The top two panels in Fig. 16 show configurations where the transmission is relatively low at all frequencies. In contrast, while the bending geometries depicted in the bottom two panels exhibit reflection peaks near  $a/\lambda \sim 0.388$ , they permit high transmission at higher frequencies. In particular, for the geometry shown in the third panel of Fig. 16, we predict over 98% transmission over the frequency range  $a/\lambda \sim 0.403-0.424$ , a bandwidth of approximately 75 nm for a PBG centered at 1.5  $\mu\text{m}$ . Figure 17 shows results for bends into vertical waveguides formed by zigzag patterns at a constant  $y$  coordinate, denoted by  $\mathbf{Z}_{y=a/2}^{YZ}$ . Again, high transmission through the bend is predicted at higher frequencies. For the geometry shown in the bottom panel of Fig. 17, over 98% transmission is predicted over the frequency range  $a/\lambda \sim 0.409-0.418$ , a bandwidth of approximately 30 nm for a PBG centered at 1.5  $\mu\text{m}$ .

V. CONCLUSION

We have demonstrated design rules for creating 3D air waveguide networks in diamondlike photonic crystals suitable for fabrication by optical phase mask or optical interference lithography. High bandwidth linear waveguides are created by removing dielectric material from the periodic PBG backbone along a path that overlaps the high light intensity

regions of the lower 3D photonic band. This suggests the possibility of combining efficient optical interference lithography techniques with highly configurable direct laser writing to produce optical microchip circuits with high density. Silicon replicas of the PBG-based circuit, exhibiting air defects in regions exposed by DLW, may be created by modifying the double-inversion technique for polymer photoresists [30]. Instead of fully infiltrating the developed photoresist with  $\text{SiO}_2$  in the first inversion step, a partial infiltration could be performed. This would result in a thin silica shell coating the SU-8 template [31].

We have designed two types of waveguide channels in the in-plane ( $x$  and  $y$ ) directions. Type I waveguides emulate the waveguide created in the familiar woodpile structure when a single rod is removed. Transmission exceeding 95% is predicted over a bandwidth of approximately 80 nm through  $x$ - $y$  bends between waveguides of this type, when the PBG is centered around 1.5  $\mu\text{m}$ . Bends between in-plane type-II waveguides, formed by creating defects in the direction perpendicular to the first type of waveguide, are predicted to allow greater than 95% transmission over a bandwidth of about 140 nm, and better than 98% transmission over a 90 nm bandwidth. We have studied bends from the in-plane waveguides into the vertical ( $z$ ) direction. For bends from type II waveguides into the vertical direction, we predict greater than 98% transmission over a bandwidth of approxi-

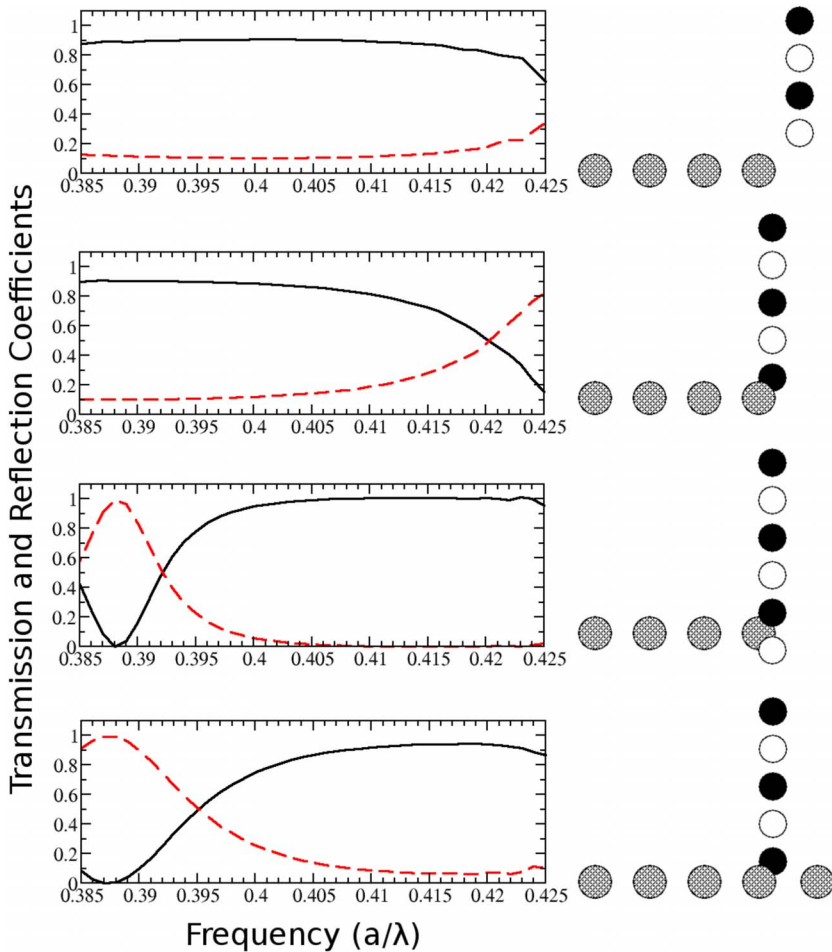


FIG. 16. (Color online) Transmission (solid, black online) and reflection (dashed, red online) spectra for bends between waveguides in the  $x$  (horizontal) and  $z$  (vertical) directions for various bend geometries. The waveguide in the  $x$  direction is denoted by  $\mathbf{X}_{a/2c/2}^{YZ}$  and the vertical waveguide by  $\mathbf{Z}_{x=3a/4}^{XZ}$  in the top panel and  $\mathbf{Z}_{x=a/4}^{XZ}$  in the other panels. The white, gray, and black circles in the schematic bend diagrams represent spherical air defects centered in the  $y=a/4$ ,  $y=a/2$ , and  $y=3a/4$  planes, respectively. The defects forming the horizontal waveguide have radius  $0.30a$  while those forming the vertical waveguide have radius  $0.25a$

mately 75 nm. In contrast to optical circuits in earlier 2D-3D PBG heterostructures [9,10], the best waveguide network architecture in the holographically defined diamond PBG material (with type-II waveguides in the  $x$  and  $y$  directions and a zigzag waveguide in the vertical direction) does not occur within planar 2D microchip layers. Instead, the identical  $x$ - and  $y$ -direction waveguide channels in the holographic architecture are offset by a quarter of a lattice constant in the third dimension. Truly planar bends between nonidentical  $x$ - and  $y$ -direction waveguides can be formed, but these exhibit mediocre transmission characteristics. As a result, it may be

more complicated to adapt defects and circuit elements from 2D PC microchips to the holographic architecture than to a 2D-3D heterostructure. On the other hand, the overall synthesis of 3D circuits of light in holographically defined PBG materials may involve fewer fabrication steps than required in previously considered 2D-3D PBG heterostructures.

These results suggest an alternative paradigm for (3+1)-dimensional integrated optics [10] in which optical components can be integrated in three geometrical dimensions as well as an additional dimension of frequency bandwidth. Unlike planar electronic microcircuits that carry a

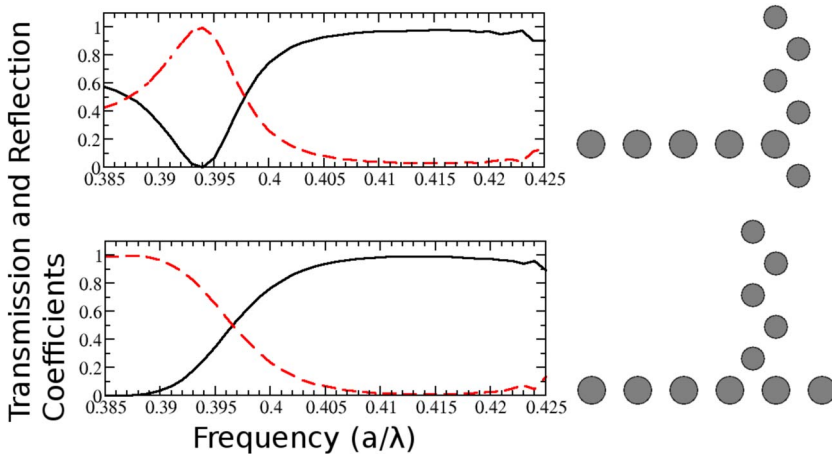


FIG. 17. (Color online) Transmission (solid, black online) and reflection (dashed, red online) spectra for bends between waveguides in the  $x$  (horizontal) and  $z$  (vertical) directions for various bend geometries. The waveguide in the  $x$  direction is denoted by  $\mathbf{X}_{a/2c/2}^{YZ}$  and the vertical waveguide by  $\mathbf{Z}_{y=a/2}^{YZ}$ . The spherical air defects are centered in the  $y=a/2$  plane. The horizontal and vertical waveguides are formed by air defects with radius  $0.30a$  and  $0.25a$ , respectively.

single channel of information at a given time, each of the optical waveguides may conduct hundreds of parallel streams of optical information. These two additional dimensions of integration, combined with the higher speed of all-optical switching [38], can more than compensate for the larger size scale of optical circuits relative to electronic circuits to process a high density of information. The fundamental challenge in realizing such far-reaching goals is the efficient and precise synthesis of 3D photonic band gap materials. For optical lithography, a specific challenge is the

precision alignment of optical phase mask lithography [19] with direct laser writing techniques [28].

#### ACKNOWLEDGMENTS

The authors are grateful to Alongkarn Chutinan for a number of helpful discussions. This work was supported in part by the National Sciences and Engineering Research Council of Canada, the Canadian Institute for Advanced Research, and the Ontario Premier's Platinum Research Fund.

- 
- [1] Sajeev John, Phys. Rev. Lett. **53**, 2169 (1984).  
 [2] Sajeev John, Phys. Rev. Lett. **58**, 2486 (1987).  
 [3] Eli Yablonovitch, Phys. Rev. Lett. **58**, 2059 (1987).  
 [4] Atilla Mekis, J. C. Chen, I. Kurland, Shanhui Fan, Pierre R. Villeneuve, and J. D. Joannopoulos, Phys. Rev. Lett. **77**, 3787 (1996).  
 [5] Shawn-Yu Lin, Edmond Chow, Vince Hietala, Pierre R. Villeneuve, and J. D. Joannopoulos, Science **282**, 274 (1998).  
 [6] M. M. Sigalas, R. Biswas, K. M. Ho, C. M. Soukoulis, D. Turner, B. Vasiliu, S. C. Kothari, and Shawn Lin, Microwave Opt. Technol. Lett. **23**, 56 (1999).  
 [7] Alongkarn Chutinan and Susumu Noda, Appl. Phys. Lett. **75**, 3739 (1999).  
 [8] E. Yablonovitch, T. J. Gmitter, R. D. Meade, A. M. Rappe, K. D. Brommer, and J. D. Joannopoulos, Phys. Rev. Lett. **67**, 3380 (1991).  
 [9] Alongkarn Chutinan and Sajeev John, Phys. Rev. B **72**, 161316(R) (2005).  
 [10] Alongkarn Chutinan and Sajeev John, Opt. Express **14**, 1266 (2006).  
 [11] V. Berger, O. Gauthier-Lafaye, and E. Costard, J. Appl. Phys. **82**, 60 (1997).  
 [12] M. Campbell, D. N. Sharp, M. T. Harrison, R. G. Denning, and A. J. Turberfield, Nature (London) **404**, 53 (2000).  
 [13] Satoru Shoji and Satoshi Kawata, Appl. Phys. Lett. **76**, 2668 (2000).  
 [14] Chaitanya K. Ullal, Martin Maldovan, Meinhard Wohlgenuth, Edwin L. Thomas, Christopher A. White, and Shu Yang, J. Opt. Soc. Am. A **20**, 948 (2003).  
 [15] D. N. Sharp, A. J. Turberfield, and R. G. Denning, Phys. Rev. B **68**, 205102 (2003).  
 [16] Ovidiu Toader, Timothy Y. M. Chan, and Sajeev John, Phys. Rev. Lett. **92**, 043905 (2004).  
 [17] Xianyu Ao and Sailing He, Opt. Express **12**, 978 (2004).  
 [18] Ovidiu Toader, Timothy Y. M. Chan, and Sajeev John, Appl. Phys. Lett. **89**, 101117 (2006).  
 [19] Timothy Y. M. Chan, Ovidiu Toader, and Sajeev John, Phys. Rev. E **73**, 046610 (2006).  
 [20] Atilla Mekis, Shanhui Fan, and J. D. Joannopoulos, Phys. Rev. B **58**, 4809 (1998).  
 [21] C. Manolatu, Steven G. Johnson, Shanhui Fan, Pierre R. Villeneuve, H. A. Haus, and J. D. Joannopoulos, J. Lightwave Technol. **17**, 1682 (1999).  
 [22] O. Painter, J. Vučković, and A. Scherer, J. Opt. Soc. Am. B **16**, 275 (1999).  
 [23] Alongkarn Chutinan and Susumu Noda, Phys. Rev. B **62**, 4488 (2000).  
 [24] Zhi-Yuan Li and Kai-Ming Ho, J. Opt. Soc. Am. B **20**, 801 (2003).  
 [25] Susumu Noda, Tatsuhiro Tomoda, Noritsugu Yamamoto, and Alongkarn Chutinan, Science **289**, 604 (2000).  
 [26] Alongkarn Chutinan, Sajeev John, and Ovidiu Toader, Phys. Rev. Lett. **90**, 123901 (2003).  
 [27] Alongkarn Chutinan and Sajeev John, Phys. Rev. E **71**, 026605 (2005).  
 [28] M. Deubel, M. Wegener, S. Linden, G. von Freymann, and S. John, Opt. Lett. **31**, 805 (2006).  
 [29] Hong-Bo Sun, Atsushi Nakamura, Koshiro Kaneko, Satoru Shoji, and Satoshi Kawata, Opt. Lett. **30**, 881 (2005).  
 [30] N. Tétrault, G. von Freymann, M. Deubel, M. Hermatschweiler, F. Pérez-Willard, S. John, M. Wegener, and G. A. Ozin, Adv. Mater. (Weinheim, Ger.) **18**, 457 (2006).  
 [31] Martin Hermatschweiler, Alexandra Ledermann, Geoffrey A. Ozin, Martin Wegener, and Georg von Freymann, Adv. Funct. Mater. **17**, 2273 (2007).  
 [32] K. M. Ho, C. T. Chan, and C. M. Soukoulis, Phys. Rev. Lett. **65**, 3152 (1990).  
 [33] Allen Taflove and Susan C. Hagness, *Computational Electrodynamics: The Finite-Difference Time-domain Method*, 2nd ed. (Artech House, Norwood, 2000).  
 [34] Virginie Lousse, Jonghwa Shin, and Shanhui Fan, Appl. Phys. Lett. **89**, 161103 (2006).  
 [35] H. S. Sözüer and Jonathan P. Dowling, J. Mod. Opt. **41**, 231 (1994).  
 [36] K. M. Ho, C. T. Chan, C. M. Soukoulis, R. Biswas, and M. Sigalas, Solid State Commun. **89**, 413 (1994).  
 [37] Amnon Yariv, Yong Xu, Reginald K. Lee, and Axel Scherer, Opt. Lett. **24**, 711 (1999).  
 [38] Dragan Vujic and Sajeev John, Phys. Rev. A **76**, 063814 (2007).  
 [39] Li and Ho also studied a so-called “type-I  $Y$ ” waveguide, whose central axis is shifted by  $a/4$  in the  $x$  direction relative to the waveguide presented here. This alternate waveguide channel studied by Li and Ho exhibits double-mode operation throughout most of the frequency range. In the field distribution picture we use here, this double-mode behavior can be explained by noting that such a waveguide channel will disturb two of the high-intensity regions in each unit cell.